Engineering Fracture Mechanics 344 (2026) 112296

Contents lists available at ScienceDirect

Engineering Fracture Mechanics

journal homepage: www.elsevier.com/locate/engfracmech

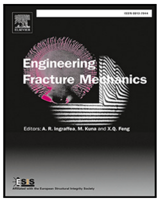

Characterisation of rate-dependent mode-II adhesive debonding based on a novel load–displacement curve parametrisation

Damjan Jurković [a], Leo Škec [a], Giulio Alfano [b],*

[a] Faculty of Civil Engineering, University of Rijeka, Radmile Matejčić 3, 51000 Rijeka, Croatia
[b] Department of Engineering, Brunel University of London, Kingston Lane, Uxbridge UB8 3PH, UK

ARTICLE INFO

Dataset link: Data and code

Keywords:
Adhesive joints
Mode-II delamination
ENF experiment
Fracture resistance
Rate-dependent behaviour

ABSTRACT

In this study, the mode-II rate dependence of an epoxy adhesive is investigated using end-notched flexure (ENF) tests conducted over loading speeds ranging from 0.1 to 5000 mm/min. To address the pronounced scatter typically observed in mode-II debonding tests, as well as the lack of a procedure for evaluation of the average load–displacement curve, a novel curve-parametrisation and statistical averaging framework is proposed. The load–displacement curves are represented using a set of parameters, enabling the construction of representative average curves for each loading speed and the quantification of parameter variability. The method allows the rate-dependent behaviour to be assessed over the entire load–displacement domain, rather than being restricted to the region typically used for the evaluation of the fracture resistance. The representative values of the critical energy release rate evaluated for each loading speed using the proposed method are in good agreement with the mean values obtained by a conventional specimen-by-specimen analysis. The results show a monotonic increase in mode-II fracture resistance with increasing loading speed, followed by a plateau at higher speeds. However, the proposed method reveals a continued monotonic evolution of the global response with loading speed, indicating that rate-dependent effects extend beyond the critical energy release rate alone. These findings demonstrate that the proposed parametrisation framework enables statistically robust characterisation of rate-dependent mode-II adhesive debonding and improved constitutive modelling.

1. Introduction

Adhesive joints are used as load-bearing structural connections in a wide range of applications in contemporary engineering. In these applications, they are subjected to a wide range of loading speeds, from creep to impact loading. Because many modern adhesives are based on synthetic polymers and are therefore sensitive to strain-rate effects, understanding their rate-dependent behaviour is of great importance. Moreover, studying adhesive debonding, as a critical failure mode of adhesive joints, is essential because it directly affects the reliability, durability and safety of adhesively bonded structures in engineering applications.

Adhesive debonding is commonly classified into three fundamental fracture modes: mode I (opening), mode II (in-plane shear) and mode III (out-of-plane shear), while practical joint failures often occur under mixed-mode loading conditions. The critical energy release rate (G_c) is a key parameter for characterising the fracture resistance of adhesive joints under different debonding modes.

---

* Corresponding author.
E-mail address: giulio.alfano@brunel.ac.uk (G. Alfano).

https://doi.org/10.1016/j.engfracmech.2026.112296
Received 6 March 2026; Received in revised form 6 May 2026; Accepted 18 May 2026

Nomenclature

$\bar{x}$	Alternative x value for a second branch function
$\hat{x}_i$	x-coordinate values for which $S_i = 0.95$, $i = (1, 2)$
a	Crack length
a_0	Initial crack length
a_e	Equivalent crack length
a_{ij}	Branch functions' fitting parameters, $i, j = (1, 2, 3)$
b	Width of adherends
C	Specimen compliance
C_0	Initial measured specimen compliance
C_{0corr}	Initial measured specimen compliance corrected for shear deformation
C_{corr}	Measured specimen compliance corrected for shear deformation
C_{msr}	Measured specimen compliance
d	Thickness of adherends
E	Young's modulus
E_f	Flexural modulus of adherends
F	Applied load
F_i	Load at the characteristic points, $i = (12, 21, 22, 31, I, M, m, N)$
f_i	Branch functions, $i = (1, 2, 3)$
G_c	Critical energy release rate
G_m	Shear modulus of adherends
$G_{II,c}$	Critical energy release rate in mode II
I	Second moment of area
k_i	Rate of change of the logistic function, $i = (1, 2)$
L	Length of adherends
L_0	Span between the supports of an ENF specimen
p_F	Second branch domain factor
R^2	Coefficient of determination
S_i	Logistic function values, $i = (1, 2)$
t	Bondline thickness
v	Prescribed displacement
w_i	Weight functions, $i = (1, 2, 3)$
x	x-coordinate value
x_i	x-coordinates of the characteristic points, $i = (12, 21, 22, 31, I, M, m, N)$
x_w	Limiting x value for a second branch function
Δa_{DPZ}	Damage process zone length of influence
ΔF	Force drop
μ_i	Midpoint of the logistic function, $i = (1, 2)$
4ENF	4-Point End-Notched Flexure
ASTM	American Society for Testing and Materials
BSI	British Standards Institution
BTBR	Beam Theory with Bending Rotations
CBBM	Compliance-Based Beam Method
CBTE	Corrected Beam Theory with Effective Crack Length
CCM	Compliance Calibration Method
DCB	Double Cantilever Beam
ELS	End-Loaded Split
ENF	End-Notched Flexure
L-BFGS-B	Limited-memory Broyden–Fletcher–Goldfarb–Shanno with Bounds
LEFM	Linear-Elastic Fracture Mechanics
MSE	Mean Squared Error
TENF	Tapered End-Notched Flexure
UTM	Universal Testing Machine

Among many test procedures proposed for the determination of mode-II critical energy release rate $G_{II,c}$, the end-notched flexure (ENF) test [1] is the most widely used. Although commonly used for determining the properties of adhesive joints [2–4], the procedure is currently standardised by the ASTM [5] and BSI standards [6] only for fibre-reinforced polymer matrix composites.

Most data-reduction schemes used to calculate the critical energy release rate G_c are based on formulations combining simple beam theory and linear-elastic fracture mechanics (LEFM). Although the industrial standard for the ENF test [5] states that the Compliance Calibration Method (CCM) is the only acceptable data reduction method for the ENF test, several different methods have been proposed (a comparison of these methods is presented in [7]). The biggest drawback of CCM is that it requires an accurate measurement of the crack length, which is not straightforward for sudden crack propagation with crack faces pressed against each other in compression, especially at higher loading speeds. In addition, the ENF test does not produce a crack whose tip can be clearly defined [8]. To avoid the measurement of the crack position, the Compliance-Based Beam Method (CBBM) [3] and the Beam Theory with Bending Rotations (BTBR) [9] for the ENF test, and the Corrected Beam Theory with Effective Crack Length (CBTE) for the ELS test [10] have been proposed for the calculation of $G_{II,c}$. An additional advantage of the CBBM method is that it does not require the measurement of any properties of the bulk material (such as Young's modulus and shear modulus) for the determination of $G_{II,c}$.

As with most topics related to adhesive joints, the rate-dependent failure behaviour has been studied more thoroughly for mode-I debonding than for mode-II and mixed-mode debonding. A widely used standardised test for mode-I debonding is the double cantilever beam (DCB) test, for which rate-dependent analyses have been performed by several authors [11–13].

Only few robust rate-dependent analyses of mode-II debonding using the ENF test have been reported in [14–19], typically within broader investigations encompassing multiple debonding modes. The rate-dependent behaviour was studied for the ENF test exclusively in [20] and for the tapered end-notched flexure (TENF) test with stable crack propagation in [21,22]. On the other hand, most of these studies rely on a relatively small number of loading speeds (typically 2 [17,18,21], 3 [14] or 4 [19,20], with the exception of Refs. [16,22] in which 5 and 6 loading speeds were employed, the latter in a TENF test setup).

There is also no clear consensus on the trend of rate-dependence of the mode-II critical energy release rate for typical adhesives, as some authors found an increase [16,17,20–22], while others found a decrease [18,23] in fracture resistance with an increase in loading speed. Moreover, it has been reported in [19] that, using the same data-reduction scheme to evaluate $G_{II,c}$ from the experimental measurements, the obtained values of $G_{II,c}$ at high-speed loads can be higher or lower than those at quasi-static loading, depending on the data acquisition method used. ENF tests that measured the strain rate in the adhesive showed that, in experiments with a constant loading speed, the strain rate in the process zone increases monotonically [14,15]. In addition, in [14] it was shown that $G_{II,c}$ increases with an increase in the strain rate.

ENF tests generally result in a lot of scatter in the load–displacement experimental data, mostly concentrated in the region after the peak load, characterised by a load drop and crack propagation. The scatter in the ENF load–displacement diagrams becomes even more problematic in rate-dependent analysis, where the diagrams of specimens tested at different loading speeds overlap, as can be seen in [19]. This issue makes the determination of the average representative load–displacement curve less straightforward than in the case of the DCB test [13]. No method has ever been proposed to produce physically realistic average load–displacement curves so far in the literature. This is probably why numerical models are commonly validated against experimental data by fitting the load–displacement diagrams of individual ENF tests or by overlapping the results of the numerical model onto the envelope of experimental results [18,19,22]. It should be noted that this kind of scatter is not an artefact of the ENF test itself, as it can also be found in alternative mode-II tests, such as the end-loaded split (ELS) and the 4-point end-notched flexure (4ENF) tests [24].

The scatter in the load–displacement diagrams also translates into the scatter of the determined values of the critical energy release rate. The typical procedure for determining a representative value of $G_{II,c}$, as defined by the ASTM standard [5] and commonly used in the literature [3,24,25], is to evaluate it for each individual specimen and then calculate the mean value and standard deviation for the entire dataset. The same methodology is also adopted for the analysis of rate-dependent experiments [16–22], where a mean value of $G_{II,c}$ is calculated in this manner for each loading speed. It should be noted that this approach for characterising the mode-II fracture resistance of adhesive joints is limited exclusively to a relatively small post-peak region of the load–displacement curve (in which most of the scatter is concentrated). However, the remaining neglected portions of the load–displacement curve contain valuable information on initial stiffness and softening and residual load-carrying capacity. As will be shown later, by ignoring these regions, important insights into the rate-dependent response and variability between specimens may be overlooked, leading to an incomplete characterisation of mode-II debonding behaviour.

In this study, ENF experiments with varying loading speeds were performed to characterise the rate-dependent mode-II fracture resistance of adhesive joints made of aluminium flat bars bonded with an epoxy adhesive. Such a comprehensive experimental dataset, comprising 29 ENF tests conducted at six loading speeds ranging from 0.1 to 5000 mm/min, provides a contribution to understanding the rate-dependent behaviour of mode-II adhesive debonding across a larger number of tested speeds than those considered in most studies, as previously discussed. In particular, by using a finer resolution of speeds, one logarithmic decade apart from each other, we can better capture the trend of rate dependence.

Although a similar experimental analysis was previously conducted to characterise mode-I rate-dependent fracture resistance using the DCB test [13], the current analysis of the experimental data revealed several issues in obtaining a reliable and accurate assessment of the rate-dependent properties of the adhesive. First, it was noticed that relatively small differences in bondline thickness, as well as bonding defects (such as voids and interfacial failure), can have a significant influence on the results. Without investigating these effects in more detail, a method has been proposed to select the most representative specimens and discard the least representative, thus significantly reducing the scatter in the experimental data.

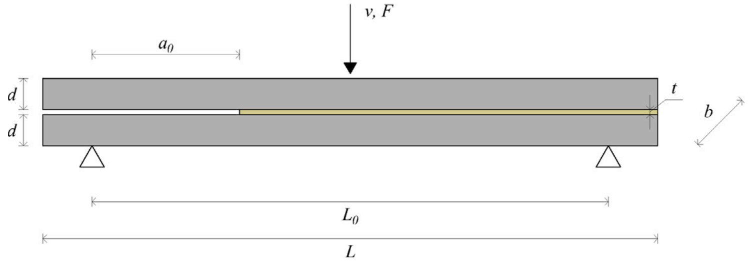

Fig. 1. ENF test specimens geometry. Dimensions are reported in Table 1.

Table 1
Dimensions of the ENF specimens.

Dimensions	L	L_0	d	b	a_0	t
Values [mm]	250	210	12.7	25.4	60	0.2

An original robust approach has been developed to parametrise the load–displacement curves, thus enabling the construction of representative average load–displacement curves. When constructed as an average for each loading speed, these curves can be used not only to directly determine the average value of $G_{II,c}$ using the common data-reduction schemes, but can also provide additional valuable information on the rate-dependent behaviour on the parts of the load–displacement curve that are typically not considered in the characterisation of the fracture resistance. Furthermore, the parametrisation of the load–displacement curve allows for its quantitative assessment, paving the way for an automated analysis of the experimental results, real-time identification of the faulty specimens and improved constitutive modelling.

The outline of the paper is as follows. The experimental set-up used is described in Section 2, while Section 3 describes the post-processing of the experimental results and the novel averaging technique based on the parametrisation of the load–displacement curve. In Section 4, the presented method is verified by comparing the mean values of the critical energy release rate from the individual specimen analyses with those obtained from the parametrised average curves. Furthermore, additional insights into the rate-dependent behaviour provided by the proposed method are analysed and discussed. The last section summarises the main original contributions of the present work and discusses its potential for application and further development.

2. Experimental set up

In order to characterise the rate-dependent behaviour of an epoxy adhesive, specimens consisting of two Al 6082-T6 aluminium plates bonded together by a thin layer of Araldite® 2015 adhesive were manufactured and tested. Note that the same materials were also used for the specimens in a former analysis of rate-dependent behaviour in mode I [13]. The specimen geometry is shown in Fig. 1, with dimensions reported in Table 1.

Specimen preparation followed the same procedure as in [13]. Bonding surfaces of the aluminium plates were roughened using sand paper and afterwards cleaned using acetone. A thin aluminium foil was used to create a clear notch edge at a distance a_0 from the left-hand support. A thin layer of adhesive was applied to the bonding surfaces using a cylindrical wooden stick and subsequently evened out using a spatula. After applying the adhesive on both plates, they were joined together and clamped on both edges. Specimens were then pressed together by applying a 60 ± 10 N force for 60 s and subsequently left to cure at room temperature for 24 h under the weight of a 1 kg mass. Both the force and the weight were evenly distributed over each specimen by means of a wooden bar. Finally, specimens were oven-cured for 60 min at 80 °C.

After curing, specimens were left to cool down and their thicknesses were measured using a digital caliper with a resolution of 0.1 mm. Because spacers were not used during specimen preparation, the bondline thickness was determined as the mean value of the difference between the total thickness of two aluminium adherends before and after bonding in three different points along the length. The resulting mean thickness was 0.19 mm, with a standard deviation of 0.06 mm. The measured bondline thicknesses of all specimens are reported in Table A.3 in Appendix A.

Experiments were performed using an electromechanical Instron 5967 universal testing machine (UTM) with 30-kN load cell (model 2580–202), except for tests at 5000 mm/min, which were performed using a 100-kN servo-hydraulic frame Instron 8501. Specimens were loaded in displacement control at six different constant loading speeds, namely 0.1, 1, 10, 100, 1000 and 5000 mm/min and at least four specimens were tested for each speed. Specimens were labelled so that the first number indicates the loading speed used for testing, while the second number indicates the chronological order of the specimen tested at that loading speed. Specimen pre-cracking was not performed.

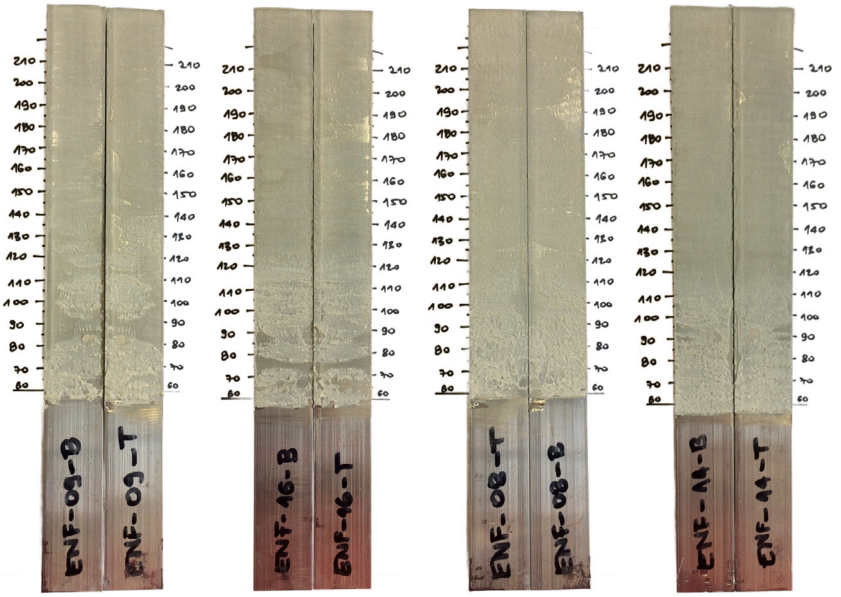

(a) 1st grade (b) 2nd grade (c) 3rd grade (d) 4th grade

Fig. 2. Representative fracture planes for each of the four bonding grades. Lower specimen grades correspond to higher amount of defects (voids and interfacial failure) and vice versa.

2.1. Fracture plane assessment

After inspection of the fracture surfaces, it was found that there are significant differences in the amount of voids and interfacial debonding present in different specimens. To account for this, visual inspection of the fracture surfaces has been performed to divide the specimens into four groups, each group characterised by a grade based on the bonding quality, with the void content decreasing from grade 1 to 4. The bonding grade structure is defined as such that each of the four grade groups contains a similar number of specimens, thus separating the dataset into quartiles. The presence of interfacial debonding was accounted for as a negative influence on the bonding quality by decreasing the bonding grade accordingly. After the grading procedure was performed for all specimens, all grade groups were cross-referenced to check for inconsistencies. The assigned bonding grades for all specimens are reported in Table A.3 in Appendix A.

Representative fracture planes for each of the bonding grades are shown in Fig. 2, where the coordinates along the length of each specimen are denoted starting from the initial crack ($a_0 = 60$ mm). It is important to note that at the end of the test the specimens were not fully detached, as for most specimens the crack reached approximately the load-application point ($a \approx 105$ mm). Specimens were therefore manually separated (in mode I), which can be recognised in fracture-surface photos by a slight difference in colour and roughness on the initial half of the crack surface. Consequently, only the initial half of the crack surface was considered for the assessment of the bonding grade. On this part of the fracture surface, the voids and interfacial failure are represented by darker areas. In case of voids, these darker areas are present symmetrically on both surfaces (top and bottom), whereas in case of interfacial failure, darker areas (representing aluminium surface) are present only on one side. The broken adhesive (by cohesive failure) is represented by lighter and rougher areas.

It can be seen that specimens in lower grades have considerably larger areas with voids and interfacial failure than those in higher grades. Using this methodology, all four grades consist of seven specimens, except for the 2nd grade, which consists of eight specimens. This resulted in a mean specimen grade equal to 2.52. The proposed grading system can be considered as a qualitative counterpart to the void volume fraction in the bondline. Such measurements, performed by digital tomography, were presented in [23], showing that an increase in bondline thickness results in a decrease in the void volume fraction and an increase in the fracture energy.

2.2. Dataset reduction

The analysis of the load–displacement curves revealed that several specimens behaved as outliers in their respective loading-rate groups. For this reason, the dataset was reduced so that each loading-rate group consisted of three representative specimens, which is assumed to be a minimum number for a representative statistical sample. Specimens were discarded from the group if: (i) their bondline thickness was significantly higher compared to the rest of the group or (ii) their bonding grade was the lowest in the group. The discarded specimens, together with the reason for their exclusion, are reported in Table A.3 in Appendix A. In the rest

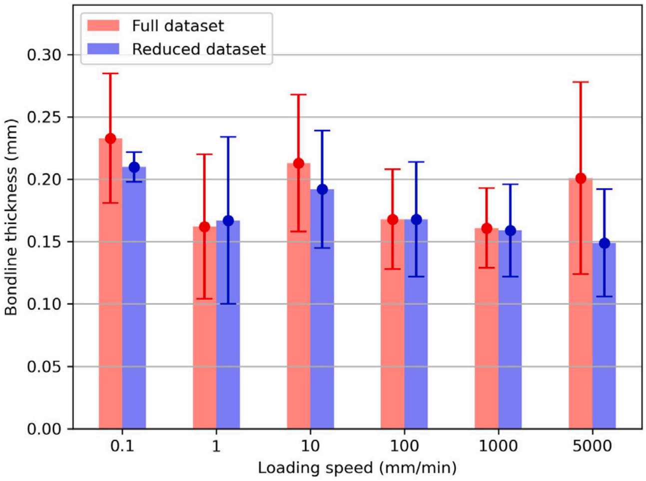

(a)

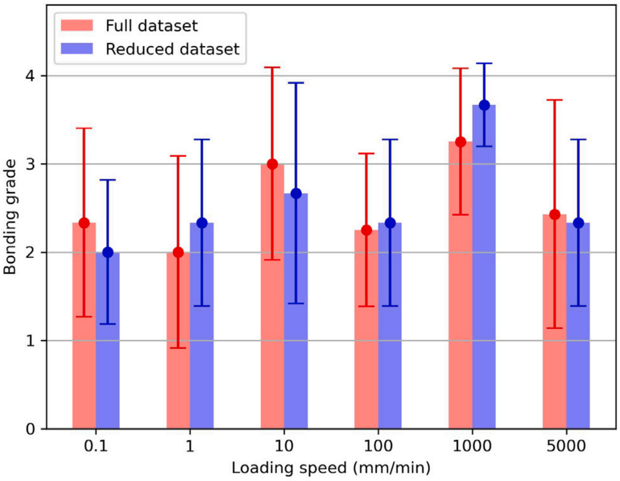

(b)

Fig. 3. Mean values of (a) bondline thickness and (b) bonding grade for each of the loading-speed groups, for both full and reduced dataset are shown. Error bars mark ± one standard deviation from the mean value.

of the paper, specimens that were not accounted for in the reduced dataset will be marked accordingly and the presented procedure will be applied to both reduced and full datasets. It should be noted that the mean bonding grade and mean bondline thickness vary across the loading-speed groups. This is true for both full and reduced datasets, whose mean values of thickness and bonding grade are shown in Fig. 3. It can be seen that the average thicknesses for different loading-speed groups in the reduced dataset are far more uniform than in the full dataset. The mean thickness of all loading-rate groups changed from 0.19 mm with a standard deviation of 0.03 mm for the full dataset to 0.17 mm with a standard deviation of 0.02 mm for the reduced dataset. When it comes to the mean bonding grade, dataset reduction process raised the mean grade for the selected specimens from 2.52 to 2.56.

2.3. *Experimental data post-processing*

From the UTM, values of the measured load and of the prescribed displacement were obtained. A characteristic load–displacement diagram is shown in Fig. 4(a). The diagram can be separated into three characteristic branches.

The first ascending branch can be in turn divided into an initial linear-elastic part and a nonlinear part due to the onset of damage in the adhesive. The very first part of this ascending branch, which is slightly nonlinear due to the initial settlement, was excluded from the analysis, as recommended by the ASTM standard [5], and below 3 kN replaced by the best linear fit of the 2

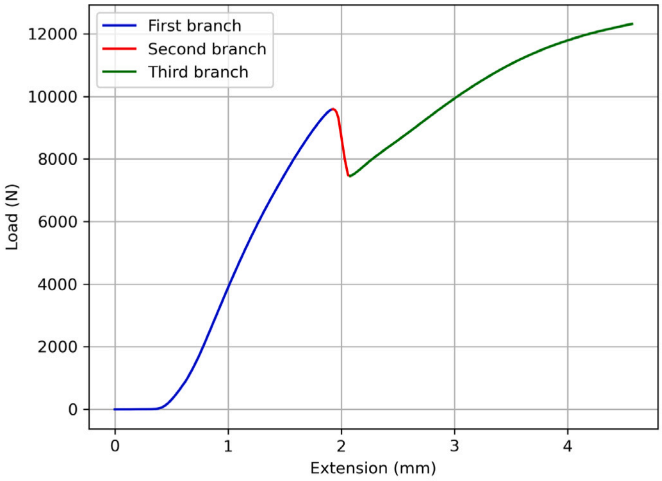

(a) 10-2 specimen

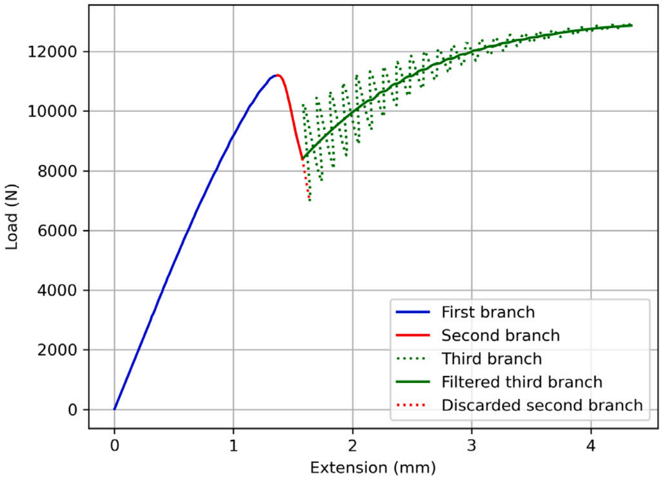

(b) 5000-3 specimen

Fig. 4. Two representative load–displacement curves with three characteristic branches for specimens tested at (a) 10 mm/min (representative for the range of speeds from 0.1 to 100 mm/min) and (b) 5000 mm/min.

to 3 kN data range. The load–displacement curve was then shifted horizontally so that its first point is located at the origin of the coordinate system. The difference between the raw and the corrected data in the first branch can be seen by comparing the blue curves in Figs. 4(a) and 4(b), respectively.

The transition from the first to the second branch, characterised by a local maximum, corresponds to further development of the damage process zone. Within the second branch of the curve (red curves in Figs. 4(a) and 4(b)) where the load decreases, the process zone fully develops and then crack propagation starts, which can be either stable, as is the case of the tests considered here, or unstable (dynamic) [26]. The third branch (green curves in Figs. 4(a) and 4(b)) corresponds to a slowdown in crack propagation and an ascending load–displacement curve. At the end of each test, the specimens were unloaded, but this part of the load–displacement curve was omitted from the further analysis.

The UTM compliance was measured by loading a rigid steel block in three-point bending. The determined value, which was $3.52 * 10^{-5}$ mm/N, was then used to correct the measured displacements in the ENF load–displacement curves.

The results for specimens tested at 5000 mm/min differ from other data due to dynamic oscillations in the third branch, as shown by the green dashed line in Fig. 4(b). 5000 mm/min data were acquired with a sampling rate of 5 kHz. To obtain a curve shape consistent with those observed at other loading speeds, the third branch was filtered using the Savitzky–Golay convolution [27] with an 81 data-point window and a second order polynomial. By doing this, the underlying shape of the load–displacement diagram in

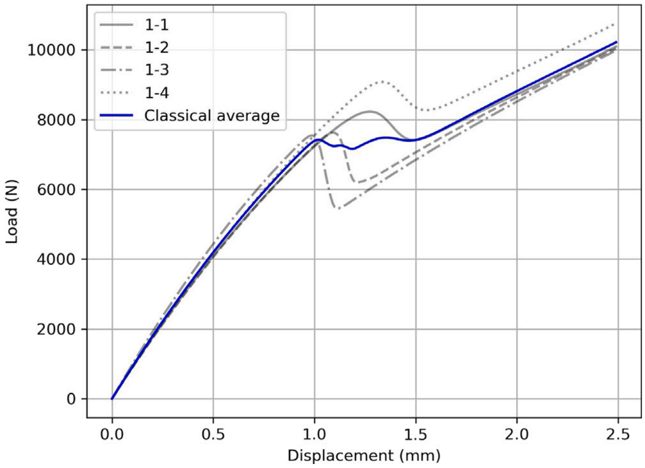

Fig. 5. Load–displacement curves for specimens tested at 1 mm/min. The classical averaging method by taking the mean value of the load for each displacement produces the blue curve, which is non-representative of the physics of the ENF test.

the third branch was obtained (solid green line in Fig. 4(b)). Finally, a part of the second branch below the intersection with the filtered third branch was discarded (dashed red curve in Fig. 4(b)).

In summary, the raw data from the UTM were corrected by replacing the initial non-linearities with linear data, accounting for rig compliance and, if necessary, removing the inertial effects by filtering the third branch.

3. Construction of average parametrised load–displacement curves

If load–displacement curves of four tests performed at 1 mm/min are compared (see grey curves in Fig. 5), it can be noticed that the scatter is most pronounced in the middle part (around the second branch) of the curve and is defined not only by a vertical, but also by a horizontal offset. To fully assess the rate-dependent behaviour of the adhesive in mode II in terms of the load–displacement response, this scatter needs to be accounted for by averaging the load–displacement curves for each loading speed and by quantifying the variation of results around the average response. However, computing the mean value of the curves with respect to displacements, as classically done for most cases, e.g. for the DCB test [13], results in a non-physical curve (see the blue curve in Fig. 5), which does not represent the characteristic behaviour during the ENF test with three distinctive branches. In particular, the characteristic load drop that follows the peak (the second branch), used for determining the fracture resistance in mode II, is completely lost by using such an averaging method.

To best of the author's knowledge, the problem of how to construct the average load–displacement curve for a given experimental ENF test dataset has not been raised. Knowing the shape of the average load–displacement curve for a given experimental dataset offers the possibility of analysing the rate-dependent behaviour of adhesive joints in a more rigorous and comprehensive way, as explained later in more detail. Furthermore, such average curves significantly improve and facilitate the calibration of numerical models for simulating adhesive debonding, as well as the assessment of their predictive capabilities. Motivated by this, a novel method for the calculation of an average ENF load–displacement curve, based on the curve parametrisation, is presented in the rest of this section.

3.1. Fitting procedure for the experimental data

As explained in the last section, the experimentally obtained load–displacement curve can be separated in three characteristic branches, connected by two smooth transitions. The three branches can be approximated by three non-linear functions, which we will refer to as branch functions, that intersect in proximity of local maximum and minimum values in the load–displacement curve. The linear least squares method was used to fit the three branch functions.

The first ascending branch is fitted with a quadratic function

$$f_1(x) = (a_{11} + a_{12}x)\, x, \tag{1}$$

where a_{11} and a_{12} are unknown constant parameters determined by the fitting procedure.

The analytical LEFM solution for the second descending branch in an ENF test (before the crack tip reaches the load application point) is [28]

$$\upsilon(F) = \frac{FL^3}{48EI} + \frac{(64G_{II,c}bEI)^{3/2}}{\sqrt{3}F^2}, \tag{2}$$

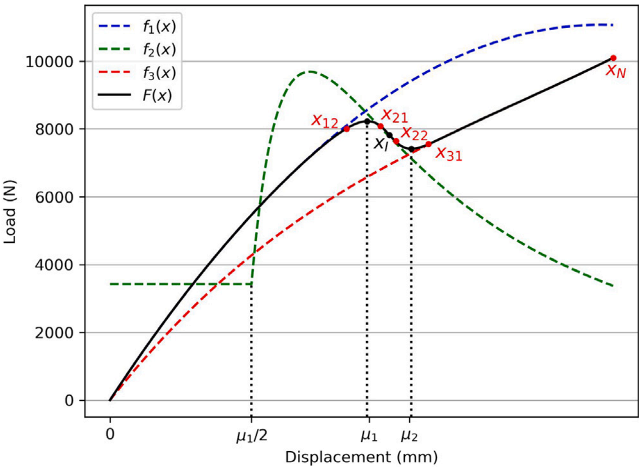

Fig. 6. Schematic of the parametrised curve $F(x)$ obtained as a weighted combination of branch functions $f_i(x)$, $i = 1, 2, 3$, with the characteristic limit points (marked in red).

but for the presented procedure an inverse function $F(v)$ is needed. To this end, the following third order negative power function was found to be the most suitable:

$$f_2(x) = a_{21}x^{-1} + a_{22}x^{-2} + a_{23}x^{-3}, \tag{3}$$

while the third ascending branch is fitted with the following cubic function:

$$f_3(x) = (a_{31} + (a_{32} + a_{33}x)\ x)\ x, \tag{4}$$

where a_{ij} ($i = 2, 3$ and $j = 1, 2, 3$) are unknown constant parameters determined by the fitting procedure. While the choice of the fitting function for the second branch is based on the analytical solution of the ENF test, it is worth noting that for the remaining two branches the polynomial expressions have been chosen based on a purely phenomenological approach, but they do reproduce the experimental response with good accuracy.

Functions $f_1(x)$, $f_2(x)$ and $f_3(x)$ are defined on the entire domain (for any $x \geq 0$). In this way, as shown in Fig. 6, they can be used to create a continuous function that captures the whole load–displacement diagram as

$$F(x) = f_1(x)w_1(x) + f_2(x)w_2(x) + f_3(x)w_3(x), \tag{5}$$

with

$$\begin{aligned} w_1(x) &= 1 - S_1(x), \\ w_3(x) &= S_2(x), \\ w_2(x) &= 1 - w_1(x) - w_3(x) = S_1(x) - S_2(x), \end{aligned} \tag{6}$$

acting as weight functions that manage the transition between the three branches (see Fig. 7a) based on a sigmoidal logistic function

$$S_i(x) = \frac{1}{1 + \exp(-k_i(x - \mu_i))}, \tag{7}$$

with $i = 1, 2$, which takes a value from the interval $\langle 0, 1\rangle$. In Eq. (7), parameters μ_i define the x-coordinates at which the logistic function takes value of 0.5, while parameters k_i govern the rate of the transition between the branches (see Fig. 7). Smaller values of k_i result in a smoother transition between the branches, while larger values result in a rapid transition. Note that k_i must be positive to ensure that the logistic function is monotonically increasing with x (as shown in Fig. 7b).

The second function, used to fit the second branch, tends to infinity (either positive or negative, depending on the parameters) as x approaches zero. If the weight function w_2 has a small, but non-zero value in this region, a global function from Eq. (5) will take a value significantly different from 0 at $x = 0$. For this reason a correction of the second function is made. Since the second function does not play an important role before the local maximum, the value of x used in the function is replaced by the value

$$\bar{x} = \begin{cases} x_w & \text{for } x < x_w \\ x & \text{for } x \geq x_w. \end{cases} \tag{8}$$

where it has been set $x_w = \mu_1/2$, see Fig. 6.

In order to fit the load–displacement curve using Eq. (5), 12 parameters in total are needed: eight parameters for the branch functions and four parameters for the transition functions. A novel curve-parametrisation algorithm was developed for this task,

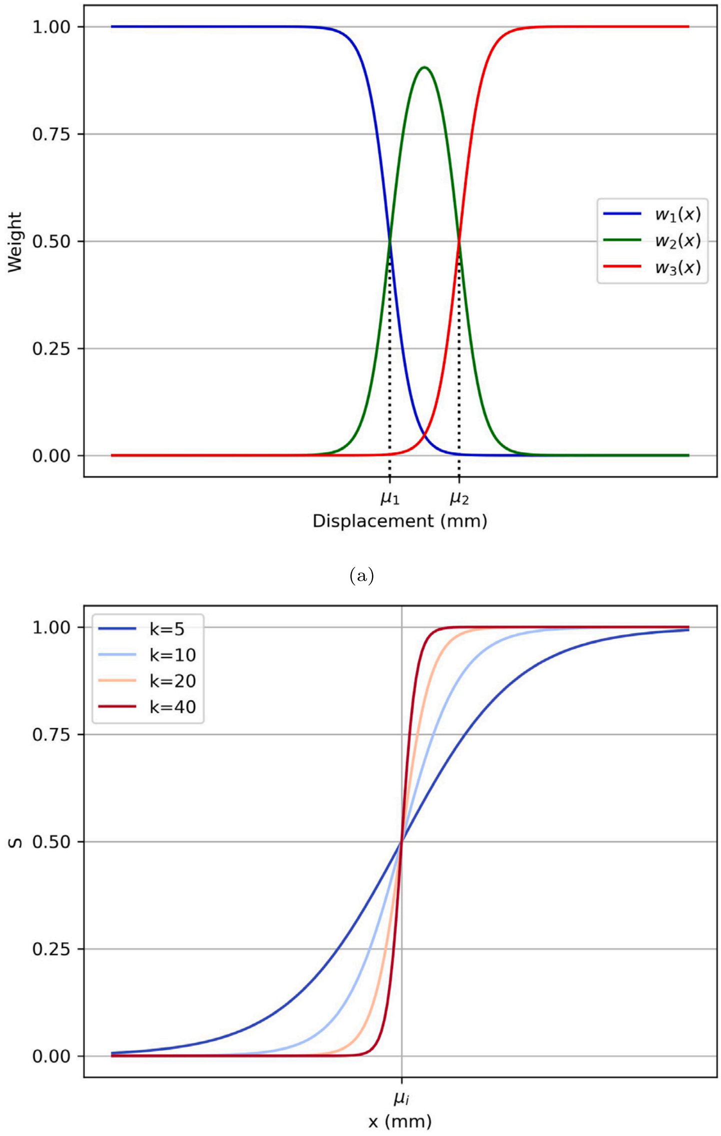

(a)

(b)

Fig. 7. Plot of: (a) weight functions $w_i(x)$ that define the transition between the branch functions $f_i(x)$, $i = 1, 2, 3$, (b) a sensitivity analysis of logistic transition functions $S_i(x)$, $i = 1, 2$.

with its flowchart shown in Fig. 9. The procedure consists of three steps: curve segmentation, curve fitting on individual segments and curve fitting on the transition region.

3.1.1. Step 1: curve segmentation

In this first step, the load–displacement data, corrected in the way explained above, is imported. The numerical first derivative of the load–displacement curve is approximated by the 2-point central difference method, and its minimal value, corresponding to the curve inflection point $(x_I,\ F_I)$, is located. Using this point, which falls within the second branch, approximately dividing it in the middle, the load–displacement curve is split into two parts. The maximum load value in the data before the inflection point corresponds to the local maximum point $(x_M,\ F_M)$, whereas the minimum load value in the data after the inflection point corresponds to the local minimum point $(x_m,\ F_m)$.

In order to obtain a good fit of the three characteristic branches, two transition regions between them need to be suitably determined and then discarded from the piecewise fitting of each branch. The limiting points of the domains on which the first and

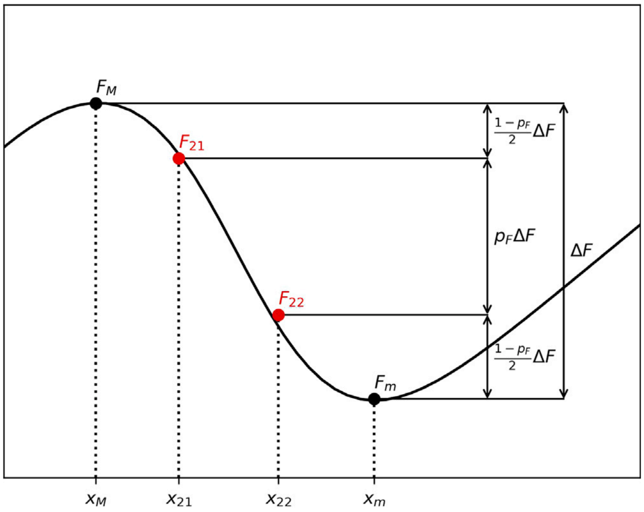

Fig. 8. Schematic representation of second branch fitting domain limits x_{21} and x_{22}.

third branches are fitted (see Fig. 6) are calculated using the x-coordinates of previously determined local extrema values as

$$\begin{aligned} x_{12} &= x_M - (x_I - x_M) = 2\,x_M - x_I \\ x_{31} &= x_m + (x_m - x_I) = 2\,x_m - x_I, \end{aligned} \tag{9}$$

essentially mirroring the distance between the local extrema points and the slope inflexion point about the local extrema.

For the specimens tested at a speed of 5000 mm/min, due to third branch filtering, the minimum point of the second branch slope F_I is not located close to the middle of the branch. Therefore, for these specimens, x_I in Eq. (9) is replaced by $0.5(x_m - x_M)$ to compute x_{12} and x_{31}.

Having determined x_{12} and x_{31} in this way, the fitting domains for the first and third branches are set as $[0, x_{12}]$ and $[x_{31}, x_N]$, respectively, where x_N is the x-coordinate of the last data point (see Fig. 6).

3.1.2. Step 2: curve fitting on the individual segments

Using the fitting domains defined in the previous step, in this second step, the linear least squares method is applied to fit the first and third branches. Fitting the first branch using Eq. (1) and third branch using Eq. (4) result in the determination of the five fitting parameters a_{11}, a_{12}, a_{31}, a_{32}, a_{33}.

To complete the piecewise fitting, the domain $[x_{21}, x_{22}]$ for fitting the second branch using Eq. (3), whose corresponding codomain is $[F_{22}, F_{21}]$ (see Fig. 8), needs to be defined. The codomain size is defined as a fraction p_F of the force drop in the second branch $\Delta F = F_M - F_m$, with $0 < p_F < 1$, so that $F_{22} - F_{21} = p_F\,\Delta F$. Therefore, F_{21} and F_{22} are given by:

$$\begin{aligned} F_{21} &= F_M - \frac{1-p_F}{2}\Delta F \\ F_{22} &= F_m + \frac{1-p_F}{2}\Delta F. \end{aligned} \tag{10}$$

The x-coordinates corresponding to F_{2i} define x_{2i}, with $i = 1, 2$, and are the limits of the second branch fitting domain. These points are shown in Fig. 8.

A decrease in parameter p_F results in a smaller fitting domain and a larger distance of its limits from the extrema points. As Eq. (3) needs to have at least three points in order to fit the second branch, for specimens with a small number of points (two or less) in the second domain, an additional one point is added on either side of the domain.

The second branch is then fitted using Eq. (3) across domain $[x_{12}, x_{21}]$ and the three additional parameters a_{21}, a_{22} and a_{23} are determined. At the end of step 2, branch functions $f_1(x)$, $f_2(x)$ and $f_3(x)$ are fully defined.

3.1.3. Step 3: curve fitting on the transition region

Global fitting using Eq. (5) is performed in this step. For this non-linear fit, a Limited-memory Broyden–Fletcher–Goldfarb–Shanno with Bounds (L-BFGS-B) non-linear optimisation algorithm [29] is used for the mean squared error (MSE) minimisation. This algorithm, which falls into the broader category of the quasi-Newton methods, is chosen because it offers a simple way to impose boundaries on the search domains of the fitting parameters, thus ensuring a convergence to a correct fit. The global fitting is performed on the domain $x \in [x_{12}, x_{31}]$ only, which means that the first and third branch parameters determined in step 2 remain constant. This allows for a smoother convergence, while the accuracy of the fit is not compromised as typically the R^2 of these branches on their respective domains is in the 0.99+ range.

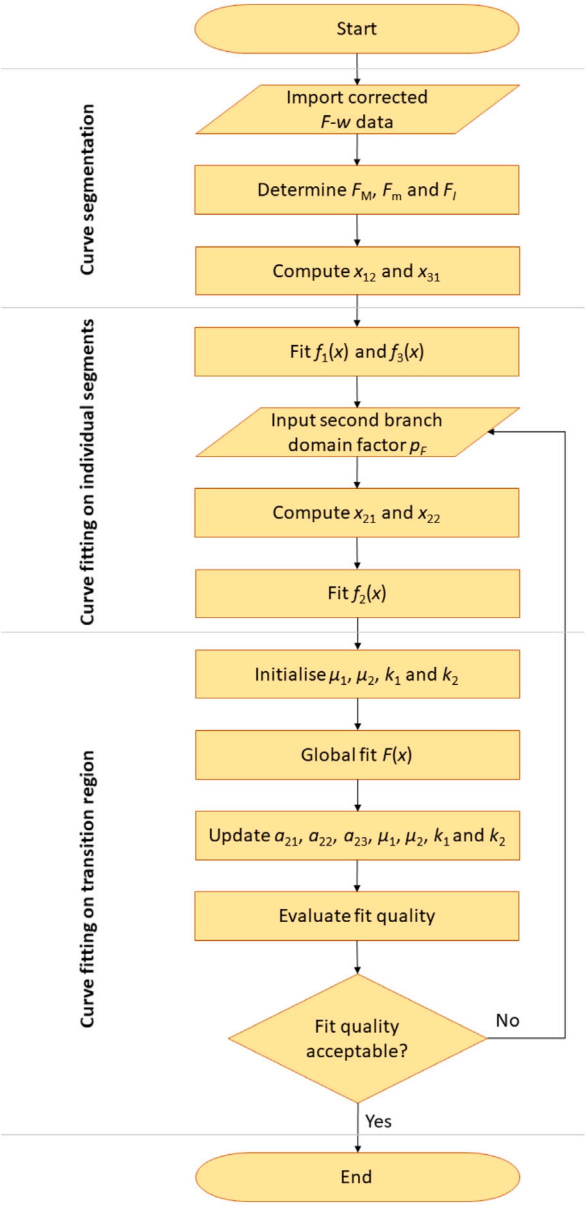

Fig. 9. Flowchart of the algorithm used for curve fitting of the experimental load–displacement data.

The parameters to be optimised are those defining the second branch (a_{21}, a_{22}, a_{23}) and the transition parameters from Eq. (7), namely μ_1, μ_2, k_1, k_2. For these 7 parameters, initial values need to be provided. For the second branch parameters, the initial values are those obtained in Step 2. The x-coordinates of the local extrema, x_M and x_m, are taken as initial values of parameters μ_1 and μ_2, respectively.

For the initial values of parameters k_i, from Eq. (7) we can derive the term for the rate of change of the logistic function

$$k_i = -\frac{\ln\left(\frac{1}{S_i(x)} - 1\right)}{x - \mu_i}, \tag{11}$$

where $x - \mu_i$ is the length on which the logistic function changes from 0.5 to $S_i(x)$. Note that function $S_i(x)$ has two asymptotes that take the values of 0 and 1, with an infinitely long transition between them (see Fig. 7b). In order to initialise k_i with a reasonable value, we set limit values of function $S_i(x)$ for which the transition between those limits takes place over a finite length. As function $S_i(x)$ is symmetric with respect to μ_i, only the upper limit values is set to 0.95, as 1 is not acceptable. Therefore, we need to define a value $\hat{x}_i$ of x for which $S_i(\hat{x}_i) = 0.95$.

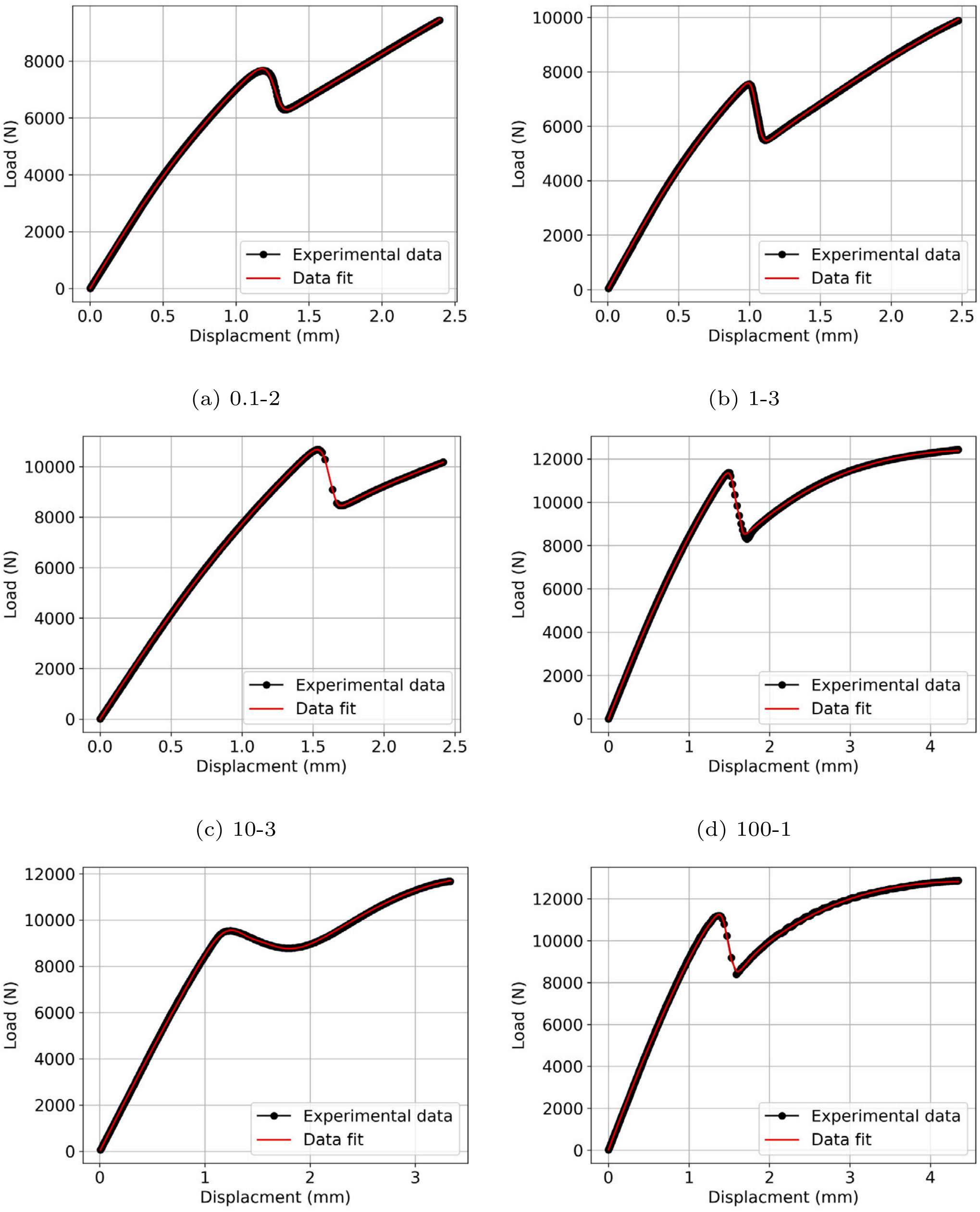

(a) 0.1-2

(b) 1-3

(c) 10-3

(d) 100-1

(e) 1000-2

(f) 5000-3

Fig. 10. Comparison of representative experimental load–displacement curves with the corresponding fitted parametrised curves for each testing speed.

Defining $\hat{x}_1 = \mu_1 + x_I - x_{12}$ and $\hat{x}_2 = \mu_2 + x_{31} - x_I$, and replacing these two values into Eq. (11) has been shown to provide values of k_1 and k_2, respectively, that lead to a stable fitting procedure and provide satisfactory accuracy of the fit.

Next, to ensure the convergence of the iterative procedure, boundaries on the search domain of the transition parameters must be set. The L-BFGS-B optimisation algorithm was chosen for its ability to set such boundaries, which in turn stabilises the fitting procedure. For the parameters μ_i, the domains are defined as $\mu_1 \in [x_{12}, x_{22}]$ and $\mu_2 \in [x_{21}, x_{31}]$. The domains on the rate of transition are set up to be $k_i \in [0, 100]$ for $i = 1, 2$, with the larger value chosen arbitrarily to ensure consistency of the parameters inside the loading-speed groups.

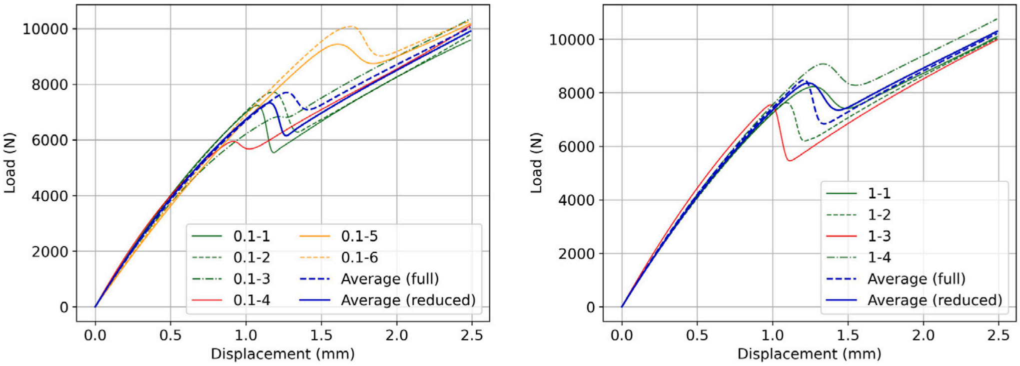

(a) 0.1 mm/min (b) 1 mm/min

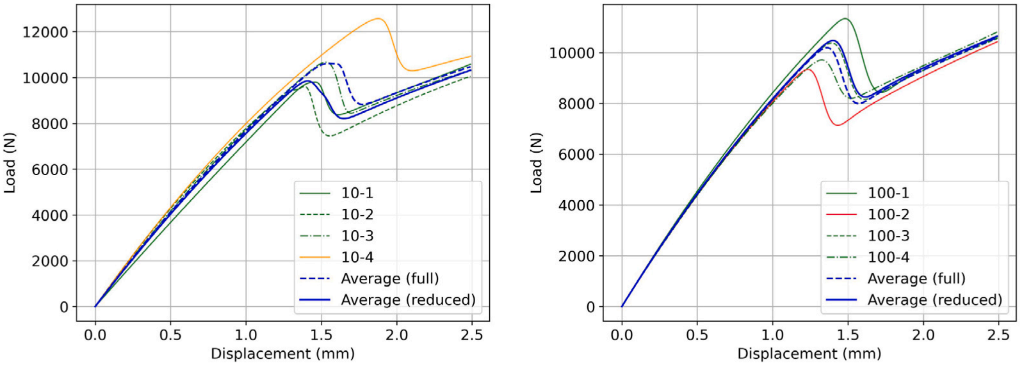

(c) 10 mm/min (d) 100 mm/min

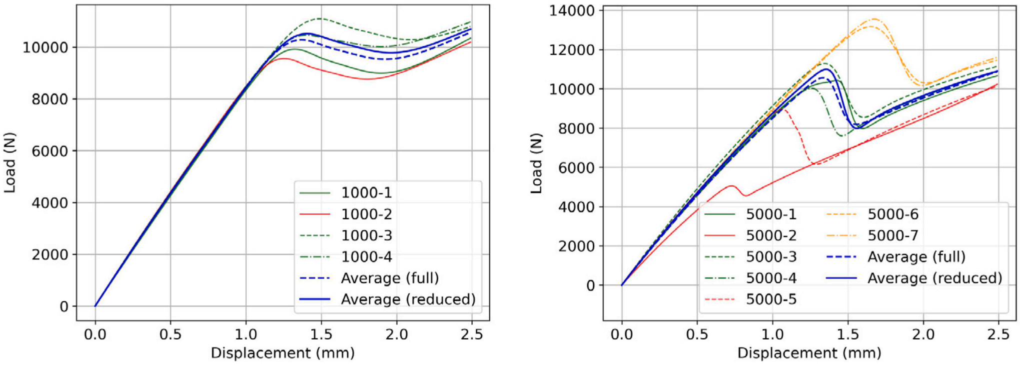

(e) 1000 mm/min (f) 5000 mm/min

Fig. 11. Individual parametrised load–displacement curves fitted from the experimental data with the corresponding parametrised average curves for each testing speed. Specimens from the reduced dataset are marked in green, those excluded due to thick bondline are marked in orange, while those excluded based on their low bonding grade are marked in red. The average curves are marked in blue (solid for the reduced dataset and dashed for the full dataset).

After the computation of the initial values and the ranges of their possible variations, global fitting is performed, resulting in new values a_{21}, a_{22}, a_{23}, μ_1, μ_2, k_1 and k_2. Using Eq. (5) and the parameters of the first and third branch functions (which did not change), a fit of the experimental data is constructed. As the value of R^2 generally takes a value of 0.99+ for the entire domain and a value of 0.97+ for the fitting domain $[x_{12}, x_{31}]$, the accuracy of the fit must be visually evaluated. In order to achieve a better fit, parameter p_F can be reduced and the procedure is repeated from the local fitting of the second branch function onward (see Fig. 9). New initial values for the second branch parameters are calculated and all other parameters, including initial values and search domain boundaries, remain unchanged. In this study a value of $p_F = 0.95$ was found to be appropriate for most specimens, with a reduction down to $p_F = 0.85$ for few specimens (0.1–3, 5000–2 and 5000–6).

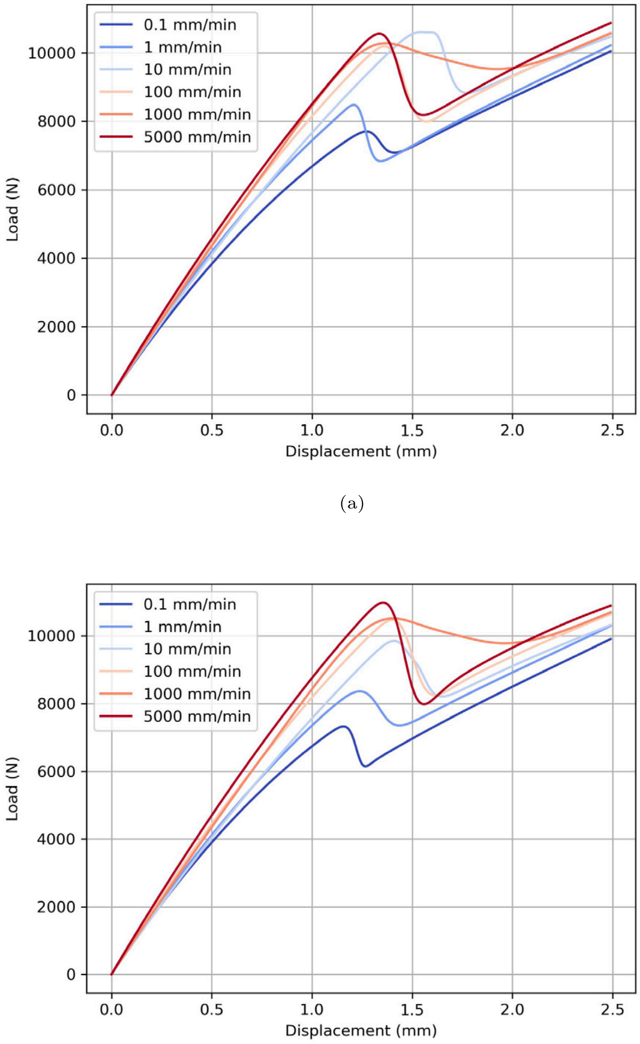

(a)

(b)

Fig. 12. Constructed average curves for all loading speeds: (a) full dataset and (b) reduced dataset.

3.1.4. Results of the fitting procedures

The representative load–displacement curves fitted from the experimental data using the procedure described above are shown in Fig. 10. A variety of different load–displacement responses are presented to illustrate the robustness of the method. It can be seen that specimens 10-3 and 100-1 had a very fast initial crack propagation, which led to a lower number of data-points recorded in the second branch. Even in such circumstances, which also appeared for other specimens tested at different speed, the proposed procedure was able to produce a robust and accurate fit. For specimens 100-1, 1000-2 and 5000-3 (amongst others), a change in the third branch, due to yielding of the aluminium adherends can be seen. On all 100 mm/min specimens, a specific bump was noticed after the local minimum on all specimens, which made the fitting of this part slightly less accurate.

3.2. Constructing the average load–displacement curves

A mean value of the parameters obtained by the fitting procedure from the previous section for all specimens tested at the same loading speed can be calculated. In this way we can construct the average ENF load–displacement curves using the global fitting Eq. (5).

The whole procedure also allows us to perform a statistical analysis on the parameters and quantify the scatter in the results. The statistical and rate-dependence analysis of the calculated parameters is given in Appendix B.

Fig. 11 shows the load–displacement curves of all ENF specimens alongside their respective average curves. In this figure, specimens which were discarded based on their large thickness are marked in orange and those discarded based on their low bonding grade are marked in red. Referring to Table A.3, it can be concluded that a low bonding grade reduces the peak load and initiates crack propagation at lower displacement values, while increasing the bondline thickness has the opposite effect. This is also consistent with the statistical analysis of the fitting parameters presented in Appendix B, where it can be observed that the parameters of the discarded specimens fall outside the error bars in Figs. B.16 and B.17. It can be noticed that parameters μ_i increase with the bondline thickness, while smaller values of k_i indicate smoother transitions between branches and thus more ductile behaviour. Specimens discarded due to their low bonding grade had the lowest values of μ_i in their respective groups, while those discarded due to their thick bondlines showed the highest values of μ_i. This indicates that a parameter analysis following the curve-fitting procedure can be used as a reliable tool for the quantitative identification of faulty specimens.

The average curves, constructed with the mean values of the parameters in Eq. (5), are shown in blue. A distinction is made between the average load–displacement curves constructed using the mean values of the parameters from the full and reduced datasets (3 specimens). It can be seen how discarding certain specimens changes the average curves.

It is obvious that all 1000 mm/min curves have a different shape than the curves loaded at different speeds. In particular, the characteristic shape of the second branch with a sudden load drop is almost completely lost. However, comparing the 1000 mm/min curves with the 100 and (filtered) 5000 mm/min curves reveals that such a behaviour cannot be attributed to the rate-dependent behaviour of the adhesive. Note that the average load–displacement curves for 100 and 5000 mm/min are very similar in shape and values, which indicates that the rate-dependent effects could be very limited in that range of speeds. In addition, the first branch, the peak and the third branch in the average load–displacement curves across 100, 1000 and 5000 mm/min are also very close to each other. Therefore, it is very likely that the 1000 mm/min load–displacement curves were affected by the machine load-cell responsiveness and data-acquisition system. Investigating the origin of this issue is outside the scope of this work. Nevertheless, because the first and third branch of the 1000 mm/min load–displacement curves are unaffected by this, these curves are still included in further analyses.

The average load–displacement curves for all loading speeds determined from the full and reduced datasets as explained above are shown in Fig. 12. It can be seen that the reduced dataset shows rate-dependent effects in a clearer and more regular way than the full dataset. Rate-dependent effects in the reduced dataset manifest in the following ways:

1. The initial stiffness increases with increasing loading speed.
2. The reduction in stiffness along the first branch becomes less pronounced with increasing loading speed.
3. The peak force increases with increasing loading speed.
4. Both extrema (maximum and minimum) on the second branch occur at larger displacement with an increase in loading speed up to 10 mm/min, after which the trend changes.
5. Force drop becomes larger with an increase in loading speed.
6. With increasing loading speed, the third branch is shifted vertically, while maintaining the same slope.

These insights into the rate-dependent behaviour in mode-II debonding would not be possible without the evaluation of average load–displacement curves using the presented methodology (Fig. 12). A similar approach could also be applied to other debonding tests exhibiting significant scatter.

4. Verification of the proposed method by critical energy release rate comparison

In this section, the accuracy of the proposed curve parametrisation method is assessed by comparing the values of the critical energy release rate evaluated using the constructed average load–displacement curves with those obtained by the standard specimen-by-specimen procedure. In both cases, the well established compliance-based beam method (CBBM) [3] was used to calculate the critical energy release rate.

4.1. Compliance-based beam method (CBBM)

CBBM employs the equivalent-crack-length concept, thus avoiding the measurement of the crack length, which, as discussed in more detail in the introduction, can be quite challenging in ENF mode-II testing. The suitability and accuracy of this method have previously been demonstrated for adhesive joints bonded with the same adhesive studied in this paper (Araldite® 2015) [3].

Assuming a simply-supported two-layer beam, as depicted in Fig. 1, with a crack length equal to a and a perfectly rigid connection along the bonded region, the specimen's compliance during the test can be calculated using simple beam theory accounting for shear effects [2] as

$$C = \frac{3a_e^3 + 2L_0^3}{8E_f bd^3} + \frac{3L_0}{10G_m bd}, \tag{12}$$

where E_f is the adherend flexural modulus calculated as

$$E_f = \frac{3a_0^3 + 2L_0^3}{8bd^3 C_{0corr}}, \tag{13}$$

G_m is the shear modulus of the arms and a_e is the equivalent crack length which accounts for the influence of the damage process zone so that

$$a_e = a + \Delta a_{DPZ} = \left(\frac{C_{corr}}{C_{0corr}} a_0^3 + \frac{2}{3} \left(\frac{C_{corr}}{C_{0corr}} - 1 \right) L_0^3 \right)^{1/3}. \tag{14}$$

In these expressions a_0 is the length of the initial crack (notch) and C_{corr} is the measured compliance C_{msr} corrected for shear deformation

$$C_{corr} = C_{msr} - \frac{3L_0}{10G_m bd}. \tag{15}$$

Note that the measured compliance is determined from the load–displacement data as the quotient of the displacement and load. The initial compliance C_0 is taken as the compliance at the beginning of the test, which in this case is constant due to the removal of the initial non-linearities from the load–displacement diagram. C_{0corr} is the value of initial compliance, corrected using Eq. (15). Now, by using the Irwin-Kies equation

$$G_{II,c} = \frac{F^2}{2b}\frac{\mathrm{d}C}{\mathrm{d}a}, \tag{16}$$

substituting C from Eq. (12) and taking the derivative with respect to a_e instead of a, the mode-II critical energy release rate is follows as

$$G_{II,c} = \frac{9F^2 a_e^2}{16b^2 d^3 E_f}. \tag{17}$$

The only material parameter required in the CBBM is the shear modulus G_m, for which, due to the limited influence on the critical energy release rate, the typical value can be used [30]. The value used in this analysis is the nominal value for Al 6082-T6 aluminium of $G_m = 26$ GPa.

4.2. Verification results and discussion

The resulting fracture-resistance curves (R-curves) calculated from the parametrised average curves for the reduced dataset are shown in Fig. 13. Energy release rate and equivalent crack length values were calculated for 0.1 mm displacement increments. The common method to calculate $G_{II,c}$ from these curves is to determine the mean value of the fracture resistance on the plateau. In this study, the plateau was defined by points where the absolute value of the gradient of the R-curve, calculated using the 2-point central finite difference method, does not exceed 0.1 N/mm^2. Points that satisfy this condition are marked in blue in Fig. 13. It can be seen that at 1000 mm/min, the R-curve increases monotonically instead of exhibiting the characteristic plateau, which is likely a consequence of the previously discussed differences in the load–displacement response.

The R-curves can also be computed for each individual specimen using their respective load–displacement curves. The representative value of the critical energy release rate is then obtained by calculating the mean of all values that make up the plateau in the R-curve, which will be indicated here as ‘standard mean’. These values are reported in Table A.3 in Appendix A. The resulting values of $G_{II,c}$ for all specimens are shown in Fig. 14 for both the full and the reduced dataset. For each loading speed, the standard mean of $G_{II,c}$ is indicated in Fig. 14 by black markers. As expected, by reducing the dataset, the scatter of the computed values of $G_{II,c}$ is reduced for each speed. The values of $G_{II,c}$ computed from the parametrised average load–displacement curves for each loading speed are indicated in Fig. 14 by dark blue markers.

Table 2 shows the values of $G_{II,c}$ calculated using the standard mean and the presented curve-parametrisation averaging method, for both the full and the reduced dataset. It can be seen that the agreement between the two approaches is very good, with the maximum relative error less than 5.5%. The proposed method yields larger values of $G_{II,c}$ than the standard mean in all cases except for the slowest speed in the full dataset.

The standard deviations calculated along with the standard mean are also reported in Table 2. As expected, the standard deviation values decreased considerably for most loading speeds by reducing the dataset.

This comparison confirms that the proposed method for determining the parametrised average load–displacement curves is very accurate and reliable. Its ability to capture the global behaviour during crack propagation for an average specimen demonstrates that the complete curve, composed of three characteristic branches, faithfully represents the average response of a group of ENF specimens. To the best of the authors’ knowledge, no method for constructing such a representative average load–displacement curve for a set of ENF tests has been proposed.

The results presented in Table 2 indicate a strongly rate-dependent behaviour of the adhesive, with significant increase in the fracture resistance for the reduced dataset from approximately 2.5 N/mm at 0.1 mm/min to values of about 4 N/mm at 5000 mm/min (not considering the higher value of about 5 N/mm at 1000 mm/min for the reasons that will be discussed later). In an analogous analysis of the mode-I rate-dependent behaviour of DCB specimens with the same adhesive and adherend material, an increase in mode-I fracture resistance was reported from approximately 0.25 to 0.55 N/mm for the same range of loading speeds [13]. As expected, the mode-II fracture resistance is much higher than that in mode-I, which can be attributed to the contribution of the effects of asperity and friction on the crack surfaces in compression [31].

To better assess the mode-II rate dependence of the tested adhesive, the change in fracture resistance with loading speed, using values of $G_{II,c}$ obtained using both methods and for both datasets, is shown in Fig. 15. It can be observed that reducing the dataset resulted in a more obvious trend in the rate-dependent behaviour of the adhesive, in which the critical energy release rate increases with the loading speed up to 1000 mm/min and then drops at 5000 mm/min. Because in the reduced dataset there is more uniformity among the specimens (in terms of the bonding grade and bondline thickness), it will be assumed that it represents the rate-dependent properties of the adhesive more accurately than the full dataset.

However, the apparent maximum of $G_{II,c}$ at 1000 mm/min should not be considered representative for the following reason. As explained earlier, in 1000 mm/min load–displacement curves (including the parametrised average curve) the characteristic force

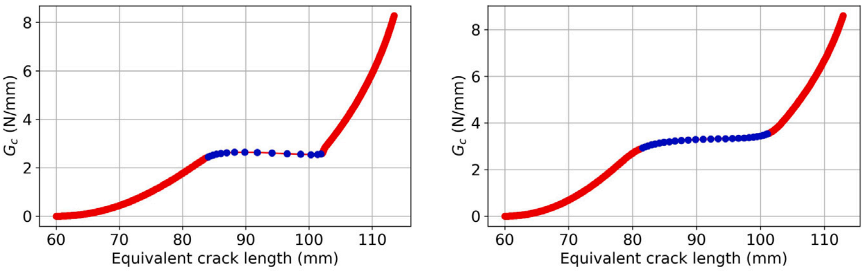

(a) 0.1 mm/min   (b) 1 mm/min

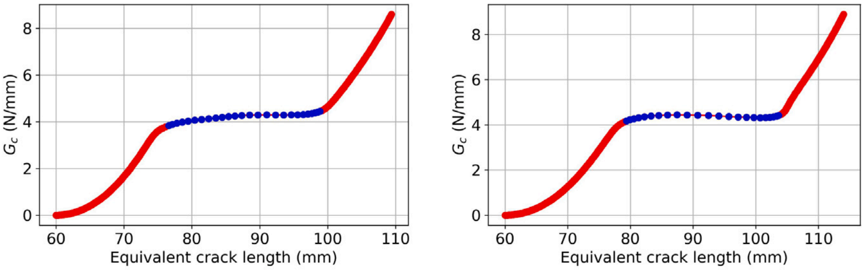

(c) 10 mm/min   (d) 100 mm/min

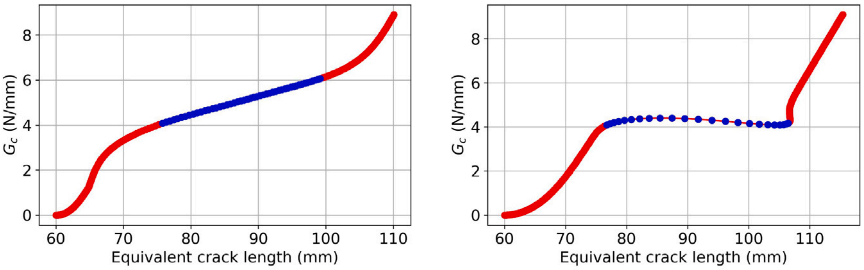

(e) 1000 mm/min   (f) 5000 mm/min

Fig. 13. R-curves calculated using the load–displacement curves obtained by the novel curve parametrisation averaging method. These curves are calculated from the reduced dataset using the CBBM data-reduction scheme.

drop after the peak is smoothed out (Fig. 11e) due to machine-induced interference in the measured response. As a result of this, the 1000 mm/min R-curves miss the characteristic plateau (Fig. 13e), which in turn results in a higher mean value of the critical energy release rate. Therefore, by comparing the parametrised average load–displacement curves (Fig. 12b) and the corresponding R-curves (Fig. 13), it seems reasonable to expect that the rate-dependent effect in the range of loading speeds between 10 and 5000 mm/min could be very limited. Consequently, a plateau, rather than a maximum at 1000 mm/min, could be expected in Fig. 15 from 10 to 5000 mm/min.

Although the previous discussion leads to the conclusion that $G_{II,c}$ reaches a plateau value of around 4 N/mm at 10 mm/min which remains approximately constant up to 5000 mm/min, there are also obvious rate-dependent effects in the first and third branches of the average load–displacement curves shown in Fig. 12. However, these branches are not taken directly into account in the data-reduction schemes used to determine the fracture resistance of the adhesive. The proposed curve parametrisation method allows for comparison of the rate-dependence across the entire domain of the average load–displacement curves. In this way, a more comprehensive rate-dependent analysis of the adhesive debonding can be performed, accounting for the increase of both the initial stiffness in the first branch and the post-fracture load-bearing capacity in the third branch.

5. Conclusion

In this work, a novel methodology was developed for assessing the rate-dependent behaviour of mode-II adhesive debonding using the ENF test. The experimental load–displacement data were analysed using a novel automatic curve-parametrisation method that can be easily employed to construct representative average curves using the mean values of the fitting parameters. The accuracy

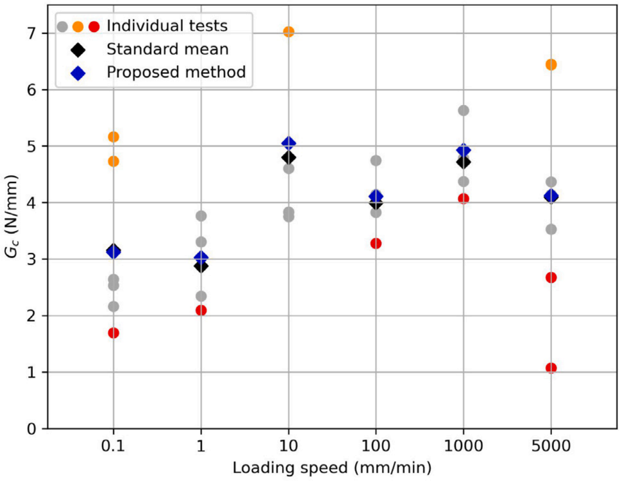

(a)

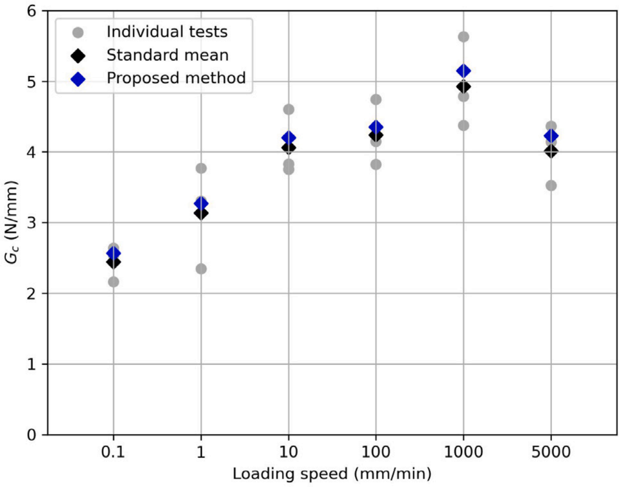

(b)

Fig. 14. Comparison of critical energy rates obtained from experimental data and from the presented curve parametrisation averaging method: (a) full dataset and (b) reduced dataset. For the full dataset specimens discarded for their bondline thickness are marked orange and those discarded for their low bonding grade are marked red. Note that the two highest values for 5000 mm/min overlap.

of the method was successfully verified by comparing the values of the critical energy release rate for each loading-speed group computed from the average parametrised load–displacement curves with those obtained using the standard specimen-to-specimen analysis.

The presented method has been applied to study the rate dependence of adhesive joints made of aluminium arms bonded with Araldite® 2015 adhesive tested at six different loading speeds ranging from 0.1 to 5000 mm/min. Using the standard approach for assessing the mode-II rate-dependent fracture resistance, $G_{II,c}$ was found to increase from approximately 2.5 N/mm at 0.1 mm/min to 4.2 N/mm at approximately 10 mm/min, after which it reaches a plateau. However, the parametrised average load–displacement curves constructed for each loading speed indicated that the rate-dependent effects have a monotonically increasing trend in parts of the load–displacement curves that were not considered for evaluation of $G_{II,c}$. In particular, the initial stiffness, peak load and post-peak bearing capacity showed an increase with increasing the loading speed.

The proposed procedure to determine average load–displacement curves for ENF tests, for which to the best of the authors' knowledge no other method had previously been proposed in the literature, offers several benefits when compared to the standard procedure of fracture characterisation based solely on the evaluation of the critical energy release rate. In particular:

Table 2
Average values of $G_{II,c}$, calculated as standard mean and using presented curve parametrisation averaging method for full and reduced datasets.

Full dataset				
Loading speed (mm/min)	Standard mean (N/mm)	Standard deviation (N/mm)	Proposed method (N/mm)	Relative error (%)
0.1	3.155	1.309	3.121	−1.071
1	2.878	0.683	3.026	5.171
10	4.802	1.324	5.052	5.200
100	3.998	0.531	4.107	2.711
1000	4.716	0.585	4.929	4.533
5000	4.096	1.797	4.123	0.651
Reduced dataset				
Loading speed (mm/min)	Standard mean (N/mm)	Standard deviation (N/mm)	Proposed method (N/mm)	Relative error (%)
0.1	2.446	0.204	2.570	5.057
1	3.138	0.592	3.269	4.173
10	4.062	0.385	4.204	3.496
100	4.239	0.380	4.353	2.694
1000	4.930	0.522	5.152	4.495
5000	4.013	0.355	4.230	5.418

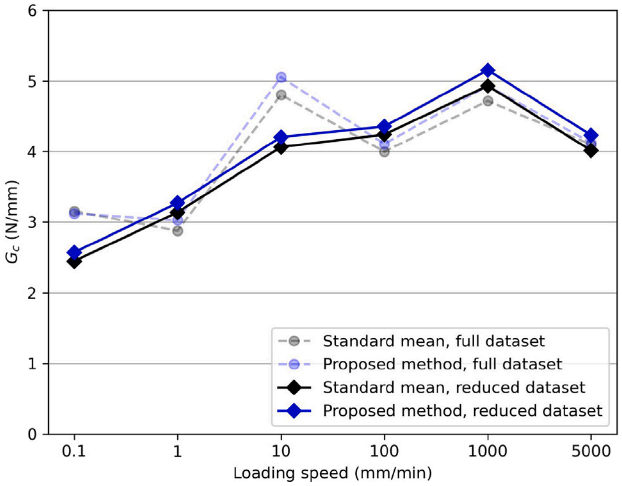

Fig. 15. Average $G_{II,c}$ values calculated for full and reduced dataset, using classical method and method presented in this paper.

1. The parametric representation of the average load–displacement curves enables a robust quantitative analysis of the scatter in the underlying data, which in turn can be used for automatic detection of specimens that deviate from the representative response.
2. The average load–displacement curves can be used as an efficient tool for a comprehensive qualitative and quantitative analysis of the rate-dependent behaviour. In particular, rate-dependent effects can also be assessed on the first and third branch of the load–displacement curve, which, as confirmed by the presented analysis, can reveal important information that is not available in case of the standard assessment of the mode-II fracture resistance. Moreover, the rate dependence can be studied at the parameter level (as illustrated in Fig. B.18).
3. For numerical simulations based on nonlinear models whose input parameters are not limited to $G_{II,c}$, for example when cohesive-zone models are used, the proposed method enables a more robust and accurate identification of the model parameters, as they allow a direct quantitative assessment of the agreement between the simulation results and the representative experimental response.
4. The determination of the average load–displacement curves also for third branch and the transition between the second and third branch can be particularly useful to evaluate the role of friction and for the parameter-identification of models that account for frictional effects [31].

The high modularity of the presented method allows for its easy modification, which can be employed for processing the results of different debonding tests, including mode-I and mixed-mode tests, as well as other types of mode-II tests, such as ELS, 4ENF and TENF. It is also worth noting that, while the methodology presented in this article is clearly not predictive, it can be used to calibrate advanced non-linear models which can indeed predict the response of complex bonded components or assemblies used in engineering applications.

Table A.3
Measured values of bondline thickness, bonding grade and $G_{II,c}$ for all specimens. Last column indicates whether the specimen was discarded from the reduced dataset, and if it was for what reason.

Loading speed (mm/min)	Specimen	Bondline thickness (mm)	Bonding grade	$G_{II,c}$ (N/mm)	Discarded (if yes why?)
0.1	1	0.200	1	2.164	No
	2	0.203	3	2.640	No
	3	0.227	2	2.535	No
	4	0.173	1	1.696	Yes, grade
	5	0.333	3	4.731	Yes, thickness
	6	0.260	4	5.164	Yes, thickness
1	1	0.163	2	3.302	No
	2	0.087	2	2.346	No
	3	0.147	1	2.095	Yes, grade
	4	0.250	4	3.767	No
10	1	0.237	3	3.830	No
	2	0.213	1	3.753	No
	3	0.127	4	4.605	No
	4	0.277	3	7.022	Yes, thickness
100	1	0.193	4	4.743	No
	2	0.170	2	3.277	Yes, grade
	3	0.103	2	4.147	No
	4	0.207	2	3.825	No
1000	1	0.140	3	4.375	No
	2	0.167	2	4.072	Yes, grade
	3	0.127	4	5.630	No
	4	0.210	4	4.785	No
5000	1	0.113	3	4.145	No
	2	0.210	1	1.071	Yes, grade
	3	0.210	3	4.366	No
	4	0.123	1	3.527	No
	5	0.137	1	2.674	Yes, grade
	6	0.320	4	6.452	Yes, thickness
	7	0.297	4	6.438	Yes, thickness

The results shown in this paper will be employed in future work that will focus on the numerical simulations of the ENF tests using cohesive-zone models that account for rate-dependence and frictional effects. Future work should also include conducting similar tests within a wider range of loading speeds to fully characterise its mode-II rate-dependence.

CRediT authorship contribution statement

Damjan Jurković: Writing – review & editing, Writing – original draft, Visualization, Validation, Software, Methodology, Investigation, Formal analysis, Data curation, Conceptualization. **Leo Škec:** Writing – review & editing, Supervision, Resources, Project administration, Methodology, Funding acquisition, Conceptualization. **Giulio Alfano:** Writing – review & editing, Supervision, Resources, Project administration, Methodology, Funding acquisition, Conceptualization.

Funding

This project has received funding from the European Union's Horizon 2020 research and innovation programme under the Marie Skłodowska-Curie grant agreement No. 701032 (MOLAY-STRUDEL). In addition, this work has been supported by the Croatian Science Foundation (HRZZ DOK-2021-02-6065) and the European Union – NextGenerationEU through a contract between the University of Rijeka and the Ministry of Science, Education and Youth of the Republic of Croatia (PU-437 uniri-iz-25-288).

Declaration of competing interest

The authors declare that they have no known competing financial interests or personal relationships that could have appeared to influence the work reported in this paper.

Appendix A. Measured values for all specimens

Table A.3 shows the measured values of bondline thickness, bonding grade and $G_{II,c}$ for all specimens, the latter calculated using the CBBM and the measured data. The last column indicates whether the specimens were discarded from the reduced dataset and specifies the reason for their exclusion (low bonding grade or thick bondline).

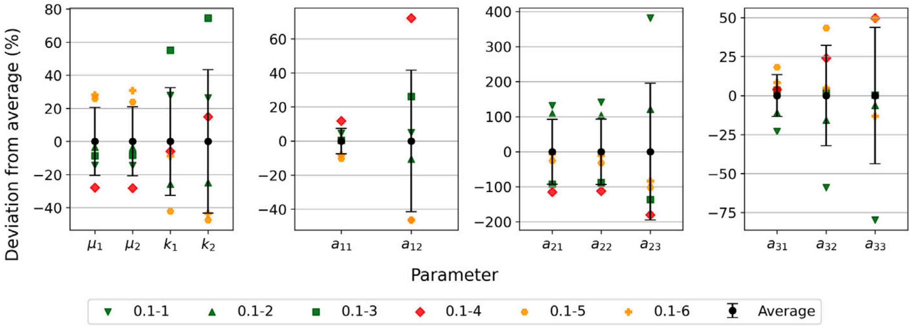

(a) 0.1 mm/min

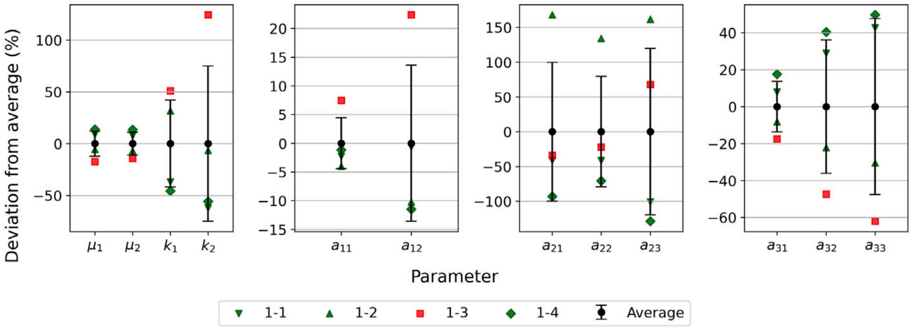

(b) 1 mm/min

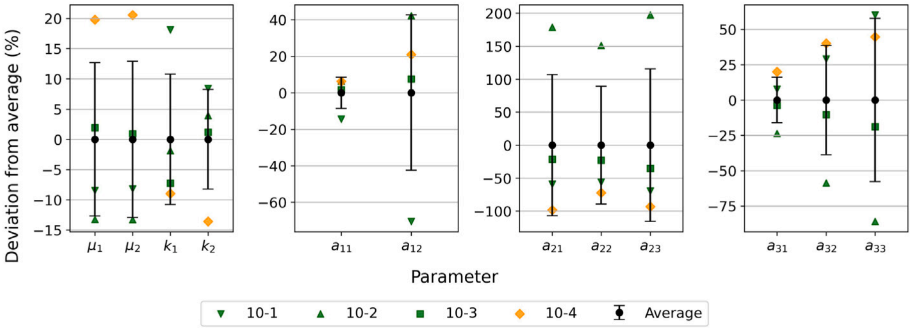

(c) 10 mm/min

Fig. B.16. Deviation from the average for the parameters used for the load–displacement curve parametrisation, separated by their respective branches for loading speed 0.1, 1 and 10 mm/min. Error bars are defined as relative standard deviations (RSD). Note the difference in deviation scales on the vertical axes.

Appendix B. Parameter analysis

To assess the variation of the fitting parameters from their respective mean, the relative deviation from the mean was calculated for each specimen. This was done for all specimens tested and the results are shown in Figs. B.16 and B.17, along with their relative standard deviation (RSD) error bars. As before, specimens which were discarded based on their large thickness are marked in orange and those discarded based on their low bonding grade are marked in red.

It can be seen that the largest scatter in the parameter values is generally in the parameters defining the second branch of the load–displacement diagram (specifically a_{21} and a_{23}). This is consistent with the scatter that can be visually assessed from Fig. 11. Furthermore, the parameters of specimens that were discarded from the full dataset are in most cases obvious outliers. The ability to identify these outliers can be used to recognise the faulty specimens during the testing process, which requires a certain number

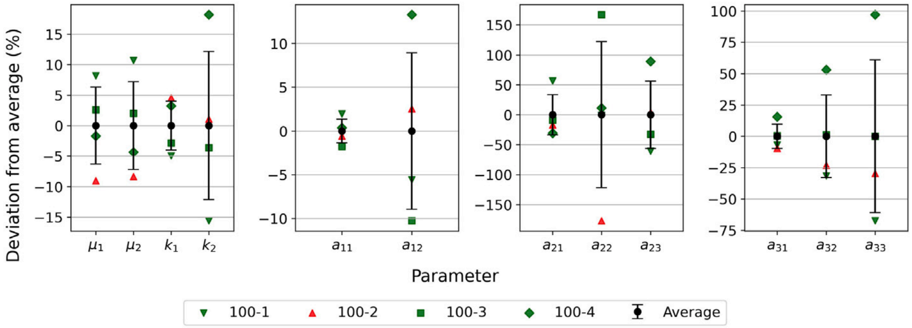

(a) 100 mm/min

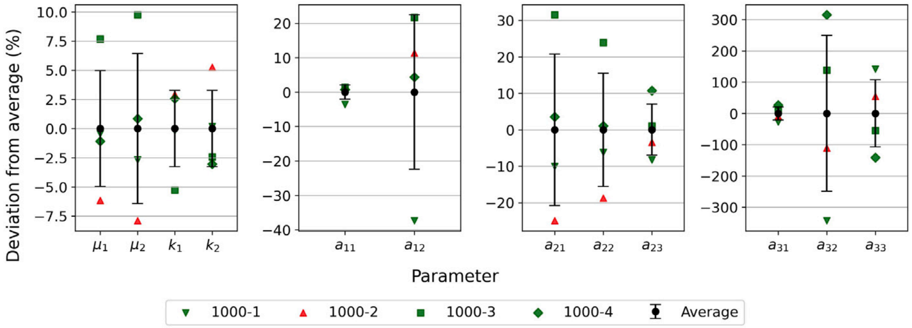

(b) 1000 mm/min

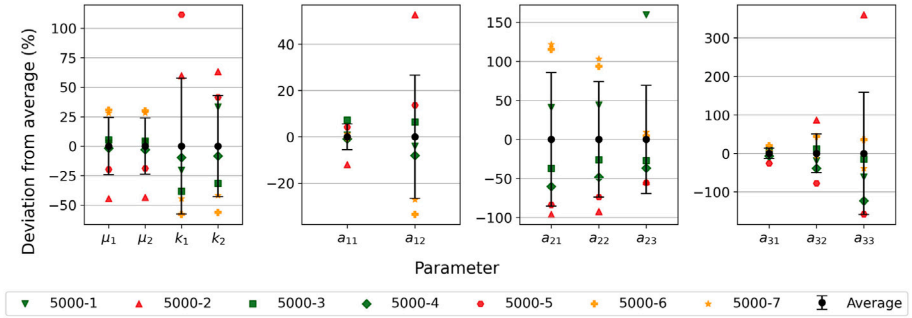

(c) 5000 mm/min

Fig. B.17. Deviation from the average for the parameters used in the load–displacement curve parametrisation, separated by their respective branches for loading speed 100, 1000 and 5000 mm/min. Error bars are defined as ± one relative standard deviation (RSD). Note the difference in the scale of the vertical axis.

of tested specimens to create a representative statistical sample. Automating this procedure could contribute to the reduction of unnecessary repeated testing by indicating the need for additional tests in real time.

The parametrisation of load–displacement curves also allows us to analyse the rate-dependence in each of the 12 parameters. The mean values of all parameters in the reduced dataset, together with their standard deviation error bars, are shown in Fig. B.18. It can be seen that the parameters defining the behaviour of the first branch, as well as the transitions between branches, show some rate-dependent trends, whereas in the second and third branch these trends are less obvious.

Data availability

Research Link Provided

Data and code (Figshare)

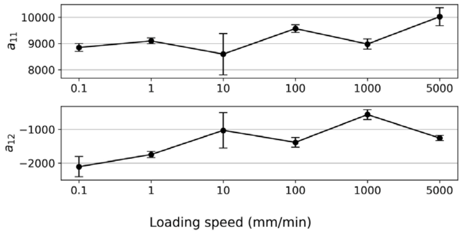

(a) First branch

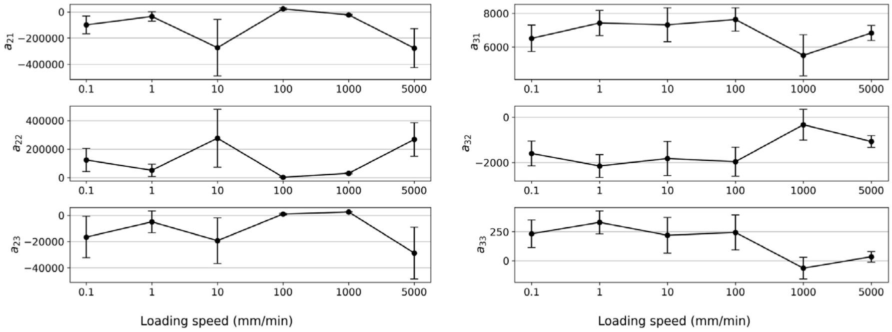

(b) Second branch

(c) Third branch

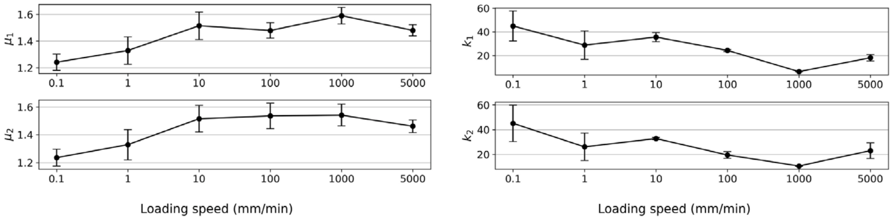

(d) Extrema points

(e) Transition smoothness

Fig. B.18. Rate-dependent effects of each of the 12 parameters for reduced dataset. Note the difference in the scale of the vertical axis.

References

[1] Russell A, Street K. Moisture and temperature effects on the mixed-mode delamination fracture of unidirectional graphite/epoxy. In: Delamination and debonding of materials. ASTM International100 Barr Harbor Drive, PO Box C700, West Conshohocken, PA 19428-2959; 1985, p. 349–70. http://dx.doi.org/10.1520/STP36314S.

[2] Wang J, Qiao P. Novel beam analysis of end notched flexure specimen for mode-II fracture. Eng Fract Mech 2004;71(2):219–31. http://dx.doi.org/10.1016/S0013-7944(03)00096-1.

[3] De Moura M, Campilho R, Gonçalves J. Pure mode II fracture characterization of composite bonded joints. Int J Solids Struct 2009;46(6):1589–95. http://dx.doi.org/10.1016/j.ijsolstr.2008.12.001.

[4] Da Silva LFM, De Magalhães FACRG, Chaves FJP, De Moura MFSF. Mode II fracture toughness of a brittle and a ductile adhesive as a function of the adhesive thickness. J Adhes 2010;86(9):891–905. http://dx.doi.org/10.1080/00218464.2010.506155.

[5] Test method for determination of the mode II interlaminar fracture toughness of unidirectional fiber-reinforced polymer matrix composites. ASTM D7905/D7905M-14, ASTM International, West Conshohocken, PA, USA; 2014.

[6] Aerospace series. Carbon fibre reinforced plastics. Test method. Determination of interlaminar fracture toughness energy. Mode II. GIIC. BS EN 6034:2015, BSI British Standards, London, United Kingdom; 2015.

[7] De Moura M, De Morais A. Equivalent crack based analyses of ENF and ELS tests. Eng Fract Mech 2008;75(9):2584–96. http://dx.doi.org/10.1016/j.engfracmech.2007.03.005.

[8] O'Brien T. Composite interlaminar shear fracture toughness, G_{IIc}: Shear measurement or sheer myth? In: Composite materials: Fatigue and fracture: 7th volume. ASTM International; 1998, p. 3–18. http://dx.doi.org/10.1520/STP13263S.

[9] Arrese A, Insausti N, Mujika F, Perez-Galmés M, Renart J. A novel experimental procedure to determine the cohesive law in ENF tests. Compos Sci Technol 2019;170:42–50. http://dx.doi.org/10.1016/j.compscitech.2018.11.031.

[10] Blackman B, Kinloch A, Paraschi M. The determination of the mode II adhesive fracture resistance, G_{IIc}, of structural adhesive joints: An effective crack length approach. Eng Fract Mech 2005;72(6):877–97. http://dx.doi.org/10.1016/j.engfracmech.2004.08.007.

[11] Blackman B, Kinloch A, Rodriguez Sanchez F, Teo W, Williams J. The fracture behaviour of structural adhesives under high rates of testing. Eng Fract Mech 2009;76(18):2868–89. http://dx.doi.org/10.1016/j.engfracmech.2009.07.013.

[12] Sun F, Zhang R, Blackman B. Determination of the mode I crack tip opening rate and the rate dependent cohesive properties for structural adhesive joints using digital image correlation. Int J Solids Struct 2021;217–218:60–73. http://dx.doi.org/10.1016/j.ijsolstr.2021.01.034.

[13] Škec L, Alfano G. Experimental and numerical study of rate-dependent mode-I failure of a structural adhesive. J Adhes 2023;99(8):1323–55. http://dx.doi.org/10.1080/00218464.2022.2106132.

[14] Carlberger T, Biel A, Stigh U. Influence of temperature and strain rate on cohesive properties of a structural epoxy adhesive. Int J Fract 2009;155(2):155–66. http://dx.doi.org/10.1007/s10704-009-9337-4.

[15] Carlberger T, Stigh U. Influence of layer thickness on cohesive properties of an epoxy-based adhesive—An experimental study. J Adhes 2010;86(8):816–35. http://dx.doi.org/10.1080/00218464.2010.498718.

[16] Blackman B, Kinloch A, Rodriguez-Sanchez F, Teo W. The fracture behaviour of adhesively-bonded composite joints: Effects of rate of test and mode of loading. Int J Solids Struct 2012;49(13):1434–52. http://dx.doi.org/10.1016/j.ijsolstr.2012.02.022.

[17] Borges C, Nunes P, Akhavan A, Marques E, Carbas R, Alfonso L, Silva L. Influence of mode mixity and loading rate on the fracture behaviour of crash resistant adhesives. Theor Appl Fract Mech 2020;107:102508. http://dx.doi.org/10.1016/j.tafmec.2020.102508.

[18] Lißner M, Alabort E, Erice B, Cui H, Blackman BRK, Petrinic N. On the dynamic response of adhesively bonded structures. Int J Impact Eng 2020;138:103479. http://dx.doi.org/10.1016/j.ijimpeng.2019.103479.

[19] Guerrero JM, González EV, Artero JA, Cimadevilla A, Rodríguez-Sereno J, Mayugo JA, De Blanpre E, Jacques V. Experimental and virtual testing of mode II and mixed mode crack propagation under dynamic loading. Int J Impact Eng 2024;193:105042. http://dx.doi.org/10.1016/j.ijimpeng.2024.105042.

[20] Feng W, Li Z, Liu B, Zhang C. Evaluation of mode II fracture toughness under high loading rate conditions for composite bonded joints. J Adhes Sci Technol 2023;37(13):1983–96. http://dx.doi.org/10.1080/01694243.2022.2110656.

[21] Marzi S. Measuring the critical energy release rate in mode II of tough, structural adhesive joints using the tapered end-notched flexure (TENF) test. Eur Phys J Spec Top 2012;206(1):35–40. http://dx.doi.org/10.1140/epjst/e2012-01584-4.

[22] May M, Hesebeck O, Marzi S, Böhme W, Lienhard J, Kilchert S, Brede M, Hiermaier S. Rate dependent behavior of crash-optimized adhesives – Experimental characterization, model development, and simulation. Eng Fract Mech 2015;133:112–37. http://dx.doi.org/10.1016/j.engfracmech.2014.11.006.

[23] Lißner M, Alabort E, Cui H, Rito R, Blackman B, Petrinic N. Experimental characterisation and numerical modelling of the influence of bondline thickness, loading rate, and deformation mode on the response of ductile adhesive interfaces. J Mech Phys Solids 2019;130:349–69. http://dx.doi.org/10.1016/j.jmps.2019.06.011.

[24] Pérez-Galmés M, Renart J, Sarrado C, Brunner A, Rodríguez-Bellido A. Towards a consensus on mode II adhesive fracture testing: Experimental study. Theor Appl Fract Mech 2018;98:210–9. http://dx.doi.org/10.1016/j.tafmec.2018.09.014.

[25] Figueiredo JCP, Campilho RDSG, Marques EAS, Machado JJM, da Silva LFM. Adhesive thickness influence on the shear fracture toughness measurements of adhesive joints. In: Special issue on joint design, Int J Adhes Adhes In: Special issue on joint design, 2018;83:15–23.http://dx.doi.org/10.1016/j.ijadhadh.2018.02.015,

[26] Alfredsson K. On the instantaneous energy release rate of the end-notch flexure adhesive joint specimen. Int J Solids Struct 2004;41(16–17):4787–807. http://dx.doi.org/10.1016/j.ijsolstr.2004.03.008.

[27] Savitzky Abraham, Golay MJE. Smoothing and differentiation of data by simplified least squares procedures. Anal Chem 1964;36(8):1627–39. http://dx.doi.org/10.1021/ac60214a047.

[28] Mi Y, Crisfield MA, Davies GAO, Hellweg HB. Progressive delamination using interface elements. J Compos Mater 1998;32(14):1246–72. http://dx.doi.org/10.1177/002199839803201401.

[29] Byrd RH, Lu P, Nocedal J, Zhu C. A limited memory algorithm for bound constrained optimization. SIAM J Sci Comput 1995;16(5):1190–208. http://dx.doi.org/10.1137/0916069.

[30] De Moura M, Silva M, De Morais A, Morais J. Equivalent crack based mode II fracture characterization of wood. Eng Fract Mech 2006;73(8):978–93. http://dx.doi.org/10.1016/j.engfracmech.2006.01.004.

[31] Serpieri R, Sacco E, Alfano G. A thermodynamically consistent derivation of a frictional-damage cohesive-zone model with different mode I and mode II fracture energies. Eur J Mech A Solids 2015;49:13–25. http://dx.doi.org/10.1016/j.euromechsol.2014.06.006.